Chemistry–A European Journal | doi.org/10.1002/chem.202004539

European Chemical Societies Publishing

Coordination Chemistry | *Hot Paper* |

Investigation of Luminescent Triplet States in Tetranuclear Cu^{I} Complexes: Thermochromism and Structural Characterization

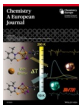

Pit Boden,[a] Patrick Di Martino-Fumo,[a] Jasmin M. Busch,[b] Florian R. Rehak,[c] Sophie Steiger,[a] Oliver Fuhr,[d] Martin Nieger,[e] Daniel Volz,[b] Willem Klopper,*[c] Stefan Bräse,*[b, f] and Markus Gerhards*[a]

Abstract: To develop new and flexible Cu^{I} containing luminescent substances, we extend our previous investigations on two metal-centered species to four metal-centered complexes. These complexes could be a basis for designing new organic light-emitting diode (OLED) relevant species. Both the synthesis and in-depth spectroscopic analysis, combined with high-level theoretical calculations are presented on a series of tetranuclear Cu^{I} complexes with a halide containing Cu_4X_4 core (X = iodide, bromide or chloride) and two 2-(diphenylphosphino)pyridine bridging ligands with a methyl group in *para* (4-Me) or *ortho* (6-Me) position of the pyridine ring. The structure of the electronic ground state is characterized by X-ray diffraction, NMR, and IR spectroscopy with the support of theoretical calculations. In contrast to the *para* system, the complexes with *ortho*-substituted bridging ligands show a remarkable and reversible temperature-dependent dual phosphorescence. Here, we combine for the first time the luminescence thermochromism with time-resolved FTIR spectroscopy. Thus, we receive experimental data on the structures of the two triplet states involved in the luminescence thermochromism. The transient IR spectra of the underlying triplet metal/halide-to-ligand charge transfer (^{3}M/XLCT) and cluster-centered (^{3}CC) states were obtained and interpreted by comparison with calculated vibrational spectra. The systematic and significant dependence of the bridging halides was analyzed.

Introduction

Luminescent transition metal complexes with binuclear Cu^{I} halide core structures have been extensively studied in the last few years, as they show remarkable photophysical properties and are very promising candidates for organic light-emitting diodes (OLEDs).[1–11] A large variety of binuclear systems with a butterfly-shaped Cu_2I_2 core unit and quantum yields of nearly 100% have been developed. These systems are capable of thermally activated delayed fluorescence (TADF) so that almost all excitons are harvested via the singlet state through reverse intersystem crossing already at room temperature. In this context, a broad range of copper complexes with 2-(diphenylphosphino)pyridine (PyrPhos) or a derivative as bridging ligand have been designed. Recently, the first binuclear Cu^{I} complexes with a synchronous singlet and triplet harvesting by combining TADF and fast phosphorescence have also been published.[7, 11, 12] It was shown that the relative contribution of both luminescence pathways can be modulated by exchanging the halides. Additionally, highly luminescent cyclic trinuclear Cu^{I} complexes have been developed.[13]

[a] *P. Boden, P. Di Martino-Fumo, S. Steiger, Prof. M. Gerhards*
Chemistry Department and Research Center Optimas, TU Kaiserslautern
Erwin-Schrödinger-Straße 52, 67663 Kaiserslautern (Germany)
E-mail: gerhards@chemie.uni-kl.de

[b] *J. M. Busch, D. Volz, Prof. S. Bräse*
Institute of Organic Chemistry (IOC), Karlsruhe Institute of Technology (KIT), Fritz-Haber-Weg 6, 76131 Karlsruhe (Germany)
E-mail: braese@kit.edu

[c] *F. R. Rehak, Prof. W. Klopper*
Institute of Physical Chemistry–Theoretical Chemistry
Karlsruhe Institute of Technology (KIT), Fritz-Haber-Weg 2
76131 Karlsruhe (Germany)
E-mail: klopper@kit.edu

[d] *Dr. O. Fuhr*
Karlsruhe Institute of Nanotechnology (INT) and Karlsruhe Nano-Micro Facility (KNMF), Karlsruhe Institute of Technology (KIT)
Hermann-von-Helmholtz-Platz 1
76344 Eggenstein-Leopoldshafen (Germany)

[e] *Dr. M. Nieger*
Department of Chemistry, University of Helsinki
P.O.Box55 (A.I. Virtasen aukio 1), 00014 Helsinki (Finland)

[f] *Prof. S. Bräse*
Institute of Biological and Chemical Systems–Functional Molecular Systems (IBCS-FMS), Karlsruhe Institute of Technology (KIT)
Hermann-von-Helmholtz-Platz 1
76344 Eggenstein-Leopoldshafen (Germany)

Supporting information and the ORCID identification numbers for the authors of this article can be found under: https://doi.org/10.1002/chem.202004539.

At the same time, analogous tetranuclear clusters have been reported, which are formally built up by combining two Cu_2I_2 subunits.[10,14–28] At this point, it is important to mention that the very first OLED based on Cu^I contained the tetranuclear complex $Cu_4(C{\equiv}Cph)_4L_2$ (L = 1,8-bis(diphenylphosphino)-3,6-dioxaoctane).[29] Lu et al. reported on a highly luminescent tetranuclear system with a Cu_4Cl_4 core and 2-(bis(2-methyl-phenyl)-phosphino)-6-methylpyridine as bridging ligand, showing a combination of TADF and fast phosphorescence at room temperature.[14] It was also shown that the luminescence properties can be tuned by modulation of the Cu_4X_4 cluster core (X = iodide, bromide, chloride) of systems with 2-(diphenylphosphino)pyridine bridging ligands[21] and coordination polymers with stair-step $[Cu_4X_4]$ fragments.[26] Thompson et al. presented a series of Cu_4I_4 clusters supported by similar P^N-type ligands (2-[(diRphosphino)methyl]pyridine) and reasoned that the emission behavior is controlled by the bulkiness of these ligands.[23]

Many years ago, Hardt et al. have already reported Cu_4I_4 clusters with pyridine ligands showing a strongly temperature dependent luminescence.[30] Deeper studies on these cubane-shaped clusters were performed later by Ford and coworkers, who applied more elaborated spectroscopic and theoretical methods.[16,31] These remarkable temperature-dependent luminescence properties are mostly known from complexes with Cu_4I_4 cubane-like core structures and monodentate phosphine or N-donating ligands.[15,17–19,22] However, luminescence thermochromism with dual phosphorescence has been observed only for a very small number of tetranuclear Cu_4X_4 clusters of approximatively octahedral shape.[23,27,28]

In this context, we developed and synthesized a series of Cu^I complexes with a Cu_4X_4 cluster core containing iodide, bromide or chloride centers and considering 2-(diphenylphosphino)-pyridine with a methyl substituent in *para* (4-Me) or *ortho* (6-Me) position of the pyridine as bridging ligands (Scheme 1). The complexes were synthesized according to protocols related to the synthetic procedures described in the literature with the ligand and the corresponding Cu^I salt as starting materials (see synthetic procedures in the Experimental Section and in the Supporting Information).[14,23] Interestingly, the differences between the luminescence properties of the neat powders of the synthesized complexes **Cu_4I_4(4-Me)$_2$**, **Cu_4I_4(6-Me)$_2$**, **Cu_4Br_4(6-Me)$_2$** and **Cu_4Cl_4(6-Me)$_2$** are already obvious by the naked eye under UV light with colors ranging from pale yellow over orange to green (Figure 1).

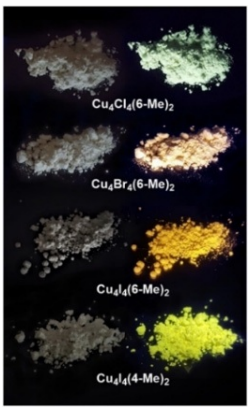

Figure 1. Powder samples of the tetranuclear Cu^I complexes at day light (left) and under UV light (right).

Intrigued by these observations and the rare luminescence thermochromism reported for some systems with Cu_4I_4 octahedral core structures, we performed thorough spectroscopic investigations in combination with high-level quantum chemical calculations to achieve a deeper understanding of these extraordinary photophysical properties. The structures of the electronic ground states were analyzed by X-ray diffraction, NMR (see descriptions in the Supporting Information, Figures S1–S6), and IR spectroscopy, in combination with theory. The temperature-dependent emission properties were characterized by static and time-resolved luminescence measurements.

The main idea was to obtain structural information on the electronically excited states involved in this thermochromism. No experimental studies in this direction have been performed so far to the best of our knowledge, as the reports only refer to theoretical calculations for this issue.[15–17]

The involved luminescent states are generally long-lived triplet states so that time-resolved step-scan FTIR spectroscopy (nanosecond to microsecond time scale) is a very suitable tool to analyze the electronically excited states. We already applied this technique successfully to a series of transition metal complexes, including several binuclear Cu_2I_2 complexes.[1,8,9,32–34] On the basis of quantum chemical calculations with respect to relative energies and molecular orbitals the high and low energy emission bands of such Cu_4I_4 clusters are assigned to transitions from triplet metal/halide-to-ligand charge transfer (^{3}M/XLCT) states and cluster-centered (^{3}CC) states to the ground state in the vast majority of cases.[10,15–19,22,23,28] For a series of presented compounds within this work the relative population of these electronically excited states can be modulated by changing the temperature. Thus these species are ideal benchmark models to separately characterize two long-lived electronically excited states of a single complex by step-scan FTIR spectroscopy.

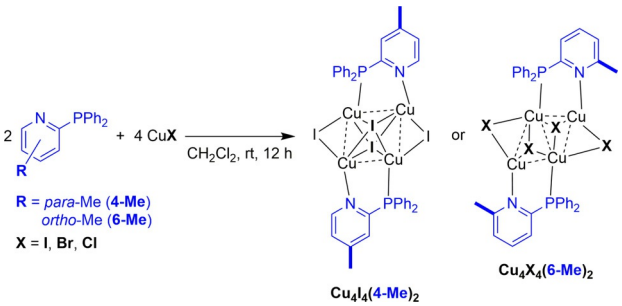

Scheme 1. Synthesis of the tetranuclear Cu^I complexes **Cu_4I_4(4-Me)$_2$**, **Cu_4I_4(6-Me)$_2$**, **Cu_4Br_4(6-Me)$_2$** and **Cu_4Cl_4(6-Me)$_2$**.

Results and Discussion

Crystallography

Molecular structures of the tetranuclear Cu^I complexes **Cu_4I_4(4-Me)$_2$**, **Cu_4I_4(6-Me)$_2$** and **Cu_4Cl_4(6-Me)$_2$** were obtained by X-ray diffraction analysis of the single crystals (Figures 2, S7–S10). In general, the copper halide core structure is held in between two methylated 2-(diphenylphosphino)pyridine bridging ligands. In both cases, the phosphorous atom of one ligand is located opposite to the nitrogen atom of the second ligand and both structures have a triclinic crystal system with space

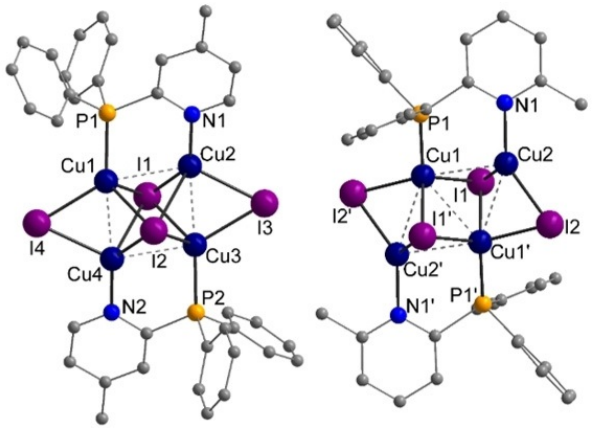

Figure 2. Molecular structures of $Cu_4I_4(4\text{-}Me)_2$ (left) and $Cu_4I_4(6\text{-}Me)_2$ (right). Hydrogen atoms and solvent molecules are omitted for clarity.

group $P\bar{1}$. While for $Cu_4I_4(4\text{-}Me)_2$ the inversion center is located in between the complexes, complex $Cu_4I_4(6\text{-}Me)_2$ is located directly on an inversion center, resulting in C_i symmetry for $Cu_4I_4(6\text{-}Me)_2$. The tetranuclear complex $Cu_4I_4(4\text{-}Me)_2$ only shows approximately C_i symmetry. All possible Cu_2I_2 subunits that can be built of the metal halide Cu_4I_4 core show the butterfly shape known from the widely investigated dinuclear PyrPhos Cu^I complex systems. Facing the tetranuclear structures by a frontal view towards the pyridine ring of the bridging ligand, iodide I1 and I2 of $Cu_4I_4(4\text{-}Me)_2$ are congruent, whereas for $Cu_4I_4(6\text{-}Me)_2$ the inner iodides I1 and I1′ are shifted outwards from the center. The iodides I1 and I2 of $Cu_4I_4(4\text{-}Me)_2$ are bridging the same four Cu^I atoms each (μ_4). In comparison, the iodides I1 and I1′ of $Cu_4I_4(6\text{-}Me)_2$ connect only three Cu^I atoms each (μ_3).

While the parallelogram which is drawn via the Cu^I atoms of $Cu_4I_4(4\text{-}Me)_2$ has angles in the range close to a rectangle, with 93.4° (Cu4-Cu1-Cu2) for one of the wider angles, the parallelogram resulting in $Cu_4I_4(6\text{-}Me)_2$ is much more stretched (57.7° up to 118.2°). Regarding the Cu–Cu distances, the values found for $Cu_4I_4(4\text{-}Me)_2$ (2.54 Å–2.76 Å) are only slightly shorter compared to $Cu_4I_4(6\text{-}Me)_2$ (2.66 Å–2.76 Å) and are in the normal range for this kind of tetranuclear complexes.[14,21] Interestingly, the Cu–Cu distances in $Cu_4I_4(6\text{-}Me)_2$ are a bit shorter compared to the chloride analogue $Cu_4Cl_4(6\text{-}Me)_2$ of this series and the literature known tetranuclear complex Cu_4Cl_4 with 6-methyl-2-bis(4-methylphenyl)pyridine as bridging ligand, both with the smaller chloride atoms.[14] In general complex $Cu_4Cl_4(6\text{-}Me)_2$ has the same core structure as the iodide complex $Cu_4I_4(6\text{-}Me)_2$ (Figures S7 and S10). For more selected parameters of the molecular structures in this study, see Tables 1, S1 and S2. Deposition Numbers 1992241, 1992242, and 2021079 ($Cu_4I_4(4\text{-}Me)_2$, $Cu_4I_4(6\text{-}Me)_2$, and $Cu_4Cl_4(6\text{-}Me)_2$, respectively), contain the supplementary crystallographic data for this paper. These data are provided free of charge by the joint Cambridge Crystallographic Data Centre and Fachinformationszentrum Karlsruhe Access Structures service www.ccdc.cam.ac.uk/structures.

Table 1. Selected molecular structural parameters of the complexes $Cu_4I_4(4\text{-}Me)_2$ and $Cu_4I_4(6\text{-}Me)_2$, bond lengths [Å] and angles [°].

$Cu_4I_4(4\text{-}Me)_2$		$Cu_4I_4(6\text{-}Me)_2$	
Lengths [Å]			
Cu1–Cu4	2.5385(18)	Cu1–Cu2′	2.6676(9)
Cu1–Cu2	2.760(2)	Cu1–Cu2	2.7483(9)
Angles [°]			
Cu4-Cu1-Cu2	93.42(6)	Cu2′-Cu1-Cu2	118.18(3)
Cu1-Cu4-Cu3	86.36(6)	Cu2-Cu1-Cu1′	57.67(3)

UV/Vis absorbance studies

All the UV/Vis absorbance spectra were measured in dichloromethane (CH_2Cl_2) under identical conditions for direct comparison. The complexes show unstructured absorbance spectra with an absorption onset at about 400 nm and weak shoulders at 300 nm and 265 nm (Figure S11). These shoulders are more pronounced for the systems $Cu_4X_4(6\text{-}Me)_2$ with 6-MePyrPhos bridging ligands than for the complex $Cu_4I_4(4\text{-}Me)_2$. The extinction coefficients increase with the halide mass but the halide exchange has almost no influence on the absorbance pattern.

For comparison with theory, the S_0 ground states of the series $Cu_4I_4(4\text{-}Me)_2$, $Cu_4I_4(6\text{-}Me)_2$, $Cu_4Br_4(6\text{-}Me)_2$ and $Cu_4Cl_4(6\text{-}Me)_2$ were optimized with density functional theory (DFT) (B3LYP-D3(BJ)/def2-TZVP), and two minimum structures were found for each complex. For all the four complexes one of these two isomers is C_i symmetric and is similar to the crystal structure (Figure 2), while the other is either open or closed butterfly-shaped (Figure 3). Throughout this work all structures with distances of 3.2 Å–3.7 Å between the N-coordinating Cu^I centers are referred to as open butterfly structures, while structures with smaller distances of 2.6 Å–2.7 Å are termed as closed butterfly. For $Cu_4I_4(4\text{-}Me)_2$, $Cu_4I_4(6\text{-}Me)_2$, $Cu_4Br_4(6\text{-}Me)_2$ and $Cu_4Cl_4(6\text{-}Me)_2$ the C_i symmetric structure is energetically higher by 5.1 kJ mol^{-1}, 11.5 kJ mol^{-1}, 20.4 kJ mol^{-1} and 27.5 kJ mol^{-1} compared to the lowest energy butterfly-shaped structure. The closed butterfly structure is the most stable one only for $Cu_4I_4(4\text{-}Me)_2$, whereas the $Cu_4X_4(6\text{-}Me)_2$ complexes yielded the open butterfly structure as the most stable isomer, according to the B3LYP-D3(BJ)/def2-TZVP optimizations. The UV/Vis spectra of both isomers for the whole series from

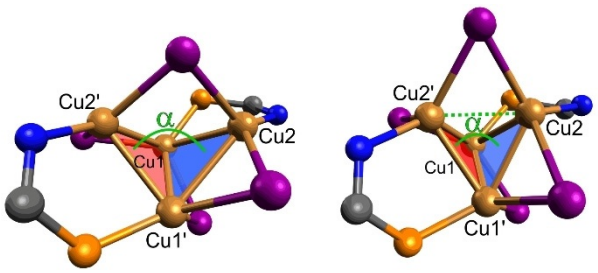

Figure 3. Open (left) and closed (right) butterfly structure of the different T_1 states of $Cu_4I_4(6\text{-}Me)_2$. While the open structure is similar to the S_0 ground state, the closed structure shows a sharper dihedral angle α and a smaller distance between Cu2′ and Cu2. (α = 97.7°/70.2°, d = 3.641 Å/2.643 Å).

Cu_4I_4(4-Me)$_2$ to **Cu_4Cl_4(6-Me)$_2$** were computed with time-dependent density functional theory (TDDFT) using CAM-B3LYP[35]/def2-TZVP (Figure S12) and the spectra of both isomers agree well with the experimental spectrum as they show absorption bands around 265 nm and 300 nm and vanish at around 400 nm. The UV/Vis spectra were also calculated within the framework of the eigenvalue self-consistent GW approximation[36] with the correlation augmented Bethe-Salpeter equation[37,38] (evGW/cBSE) and also this approach suggests similar UV/Vis spectra for both isomers (Figure S13) with bands at 265 nm and 300 nm, so a final decision on which isomer is favored in solution cannot be made based on the computed UV/Vis spectra.

Luminescence investigations at variable temperature

At first, luminescence investigations were performed in the solid state at room temperature to elucidate the influence of the halide exchange and the bridging ligands on the emission behavior. The emission spectra shown in Figure 4 were recorded in KBr matrices at an excitation wavelength of $\lambda_{ex} = 355$ nm. The complex **Cu_4I_4(4-Me)$_2$** shows a broad unstructured emission centered at 529 nm. The band shape of the luminescence of the analogue system **Cu_4I_4(6-Me)$_2$** with a methyl group in 6-position of the bridging ligand is similar but significantly redshifted to 593 nm. Surprising results were obtained upon halide exchange for the complexes **Cu_4Br_4(6-Me)$_2$** and **Cu_4Cl_4(6-Me)$_2$**, as their emission spectra show shoulders in addition to the main band. The emission maxima of the main bands of the bromide and chloride systems are localized at 600 nm and 505 nm, respectively. The shoulders, for their part, are situated at about 515 nm and 600 nm. This emission pattern is a clear sign for a dual emission from two different electronically excited states with inverted relative intensities by comparing the complexes **Cu_4Br_4(6-Me)$_2$** and **Cu_4Cl_4(6-Me)$_2$**.

Intrigued by these promising emission properties already at 290 K, we conducted temperature-dependent luminescence experiments with KBr pellets and neat films of the samples in the temperature range of 10 K–290 K.

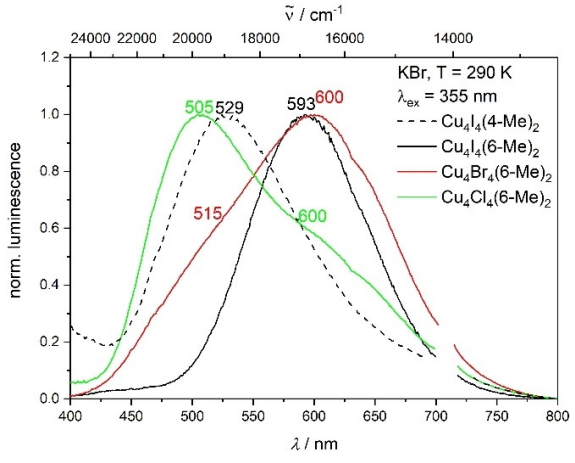

Figure 4. Solid state emission spectra (KBr) of **Cu_4I_4(4-Me)$_2$**, **Cu_4I_4(6-Me)$_2$**, **Cu_4Br_4(6-Me)$_2$** and **Cu_4Cl_4(6-Me)$_2$** recorded at 290 K with $\lambda_{ex} = 355$ nm.

The emission maximum of the complex **Cu_4I_4(4-Me)$_2$** is mostly temperature independent, as only a small blueshift of 6 nm was observed upon cooling down the sample to 10 K (Figure S17). This spectral shift may result from an inhibition of the excited state relaxation in the rigid matrix at low temperature, which is known from the literature as "rigidochromism".[39] Additionally, it should be mentioned that the characteristic redshift observed for the related binuclear Cu^I complexes showing TADF is not observed here, which is a clear indication that such a mechanism does not occur in the case of **Cu_4I_4(4-Me)$_2$**. The emission intensity more than doubles by cooling down the sample from 290 K to 10 K, which means that non-radiative deactivation channels must be efficiently inhibited at low temperature. This is also reflected by the luminescence lifetimes measured by time-correlated single-photon counting (TCSPC), which rise from 5 μs to 24 μs upon cooling (Table S4, Figures S18 and S19). As the temperature-dependent emission spectra do not agree with a TADF process, the luminescence with microsecond lifetimes over the complete temperature range (10 K–290 K) is clearly assigned to phosphorescence. In contrast, the emission behavior of the Cu_4X_4 complexes with 6-MePyrPhos bridging ligands strongly depends on temperature. For the iodide containing system **Cu_4I_4(6-Me)$_2$** the initial room temperature emission at 593 nm redshifts to 621 nm and slightly increases in intensity, when the sample is cooled down to 90 K (Figure 5 a). This shift indicates subtle changes of the electronic properties of the underlying excited state, which are attributed in literature to a shortening of the Cu···Cu bond lengths in the cluster for similar Cu_4I_4 systems with phosphine ligands.[15,19,20] At the same time, a blue emission band starts to emerge at around 500 nm, which is visible at temperatures equal to or below 130 K. At 10 K, only the blue emission is observed in the spectrum, with a maximum at 479 nm and complete disappearance of the low energy emission band. At this point, it is important to mention that the blue emission reaches an intensity that is more than four times higher than the luminescence at 290 K, which should again result from an inhibition of non-radiative deactivation processes at low temperature. The described temperature-dependent emission properties show that the system has a pronounced excited state thermochromism with two distinct emissive excited states, which are clearly separated in energy. TCSPC measurements were then performed for both emission bands, where excited state lifetimes of 16.0 μs–56.0 μs (contributing ≥95 %) were obtained for the low energy emission (emission monochromator set to 593 nm–622 nm, depending on temperature) in the temperature range of 290 K–70 K. At the same time, the blueshifted emission (emission monochromator set to 479 nm–492 nm, depending on temperature) shows time constants of 12.7 μs–19.6 μs (contributing ≥88 %) at temperatures of 70 K–10 K. These values clearly suggest dual phosphorescence from two different excited triplet states and are listed in detail in Table S5 (Figures S20 and S21). In particular, the time constants of 12.7 μs and 56 μs measured for the high and low energy bands at 70 K, where both emission bands show significant intensities, underline the presence of two isolated electronically excited states.

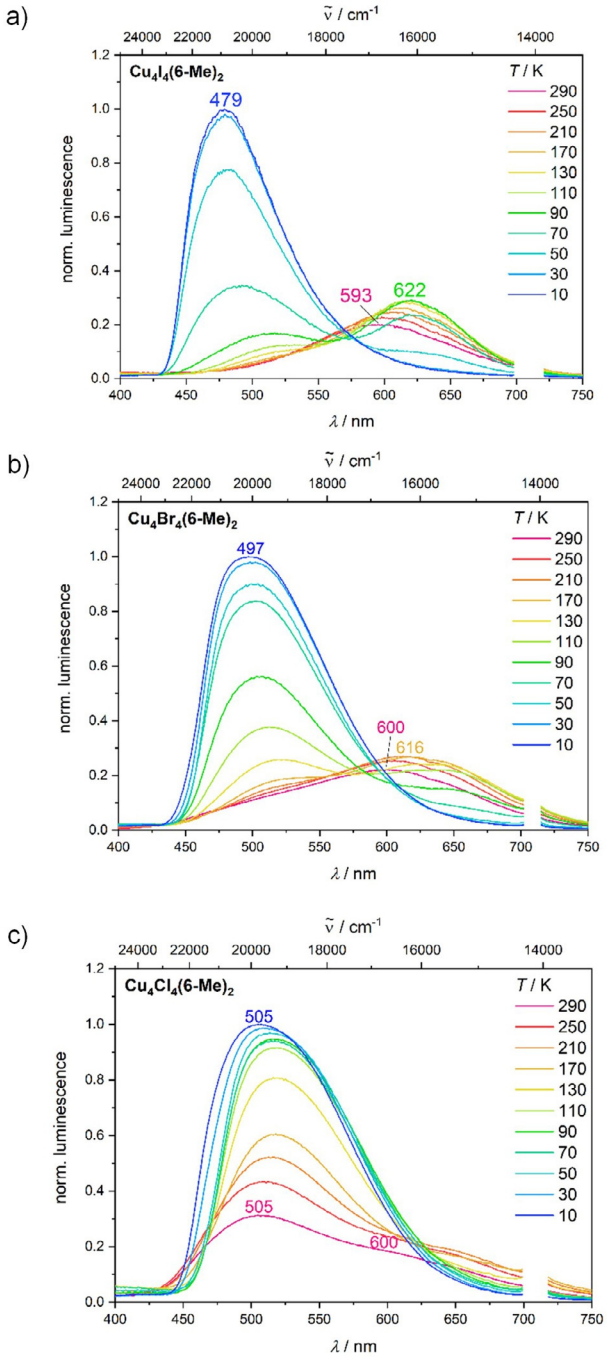

Figure 5. Emission spectra (KBr) of a) $Cu_4I_4(6\text{-Me})_2$, b) $Cu_4Br_4(6\text{-Me})_2$ and c) $Cu_4Cl_4(6\text{-Me})_2$ in the temperature range of 10 K–290 K recorded with $\lambda_{ex} = 355$ nm.

The same static and time-resolved luminescence experiments were then performed using neat films of $Cu_4I_4(6\text{-Me})_2$, where the same thermochromism was observed (Figure S22, Table S6). Hence, the influences of the matrix on the emission properties are not relevant here.

In the next step, the variable temperature luminescence studies were extended to the analogues $Cu_4Br_4(6\text{-Me})_2$ and $Cu_4Cl_4(6\text{-Me})_2$ showing dual emission in KBr already at room temperature, as described above.

For the bromide system $Cu_4Br_4(6\text{-Me})_2$ (Figure 5b), the initial room temperature emission at 600 nm also redshifts upon cooling, reaching 616 nm at 170 K. At the same time, the intensity of the mentioned blueshifted shoulder clearly increases in intensity at temperatures of 170 K and below. The low energy emission completely vanishes at 30 K, whereas the blue emission band, centered at 497 nm, reaches an intensity which is more than three times higher compared to the initial room temperature emission. The observed emission spectrum is assigned to two distinct emissive triplet states, in accordance with two mainly contributing μs-components observed at room temperature at 510 nm (2.5 μs (31%) and 15.2 μs (54%)) and 600 nm (3.6 μs (13%) and 23.0 μs (82%)) (Table S9, Figures S23 and S24). The essentially biexponential behavior results from the overlapping emission bands.

Similar behavior is also observed for the chloride complex $Cu_4Cl_4(6\text{-Me})_2$ (Figure 5c), where the low energy emission, which is weak compared to the high energy emission already at 290 K, completely vanishes at a temperature of 90 K. The TCSPC results at room temperature at 510 nm (2.2 μs (43%) and 10.0 μs (46%)) and 610 nm (2.1 μs (23%) and 16.8 μs (71%)) are assigned to dual phosphorescence (Table S10, Figures S25 and S26).

Temperature-dependent excitation spectra were recorded for the four systems by considering the corresponding emission maxima. The excitation spectra show onsets between 435 nm and 490 nm, depending on the system, temperature and the emission peak (Figures S28–S31). At low temperature, slightly higher energy UV excitation is required for an efficient population of the emissive states compared to room temperature. Considering the three dual-emissive complexes $Cu_4X_4(6\text{-Me})_2$, it should be mentioned that the excitation spectra of the high and low energy emission bands are slightly shifted relative to each other (Figures S28–S31), but that the relative intensity of the two emission bands cannot be modulated strongly by tuning the excitation wavelength.

Summarizing the variable temperature luminescence data, it can be said that all the three tetranuclear systems with 6-MePyrPhos bridging ligands show a pronounced thermochromism with two emissive triplet states, whereas only a single mostly temperature-independent emission was observed for the complex $Cu_4I_4(4\text{-Me})_2$. Hence, the luminescence behavior is strongly influenced by the position of the methyl group on the bridging ligand. The methyl group in 6-position exerts steric pressure on the Cu_4X_4 cluster (see chapters on crystallography and IR spectroscopy), which is responsible for the thermochromism. At the same time, the dual phosphorescence is not observed for the complex with 4-MePyrPhos ligands in combination with the lower steric hindrance close to the Cu_4X_4 cluster. For the series $Cu_4X_4(6\text{-Me})_2$ the halide exchange has a small but significant influence on the emission wavelengths. At room temperature, the exchange of iodide against bromide or chloride induces a redshift of the low energy emission from 593 nm to 600 nm (Figure 4). A more pronounced redshift is observed for the high energy emission at 10 K, with a shift from 479 nm for iodide to 505 nm for the chloride system. The emission band of the bromide complex appears in between

these two with a maximum at 497 nm (Figure S27). At the same time, the halide centers have a big influence on the relative intensities of high and low energy bands. Thermal energy has a huge impact on the population of the emissive triplet states according to the luminescence investigations at variable temperature. The relative intensities of the observed emission bands show that thermal energy is sufficient to induce a population of the low energy emitting triplet state at 290 K. In the case of **Cu_4I_4(6-Me)$_2$**, this low triplet state is efficiently populated, so that no high energy emission is observed at all. However, the blue emission is observed already at room temperature for **Cu_4Br_4(6-Me)$_2$** and to an even higher extent for **Cu_4Cl_4(6-Me)$_2$**, which should result from a higher energy barrier between the discussed triplet states and thus kinetic trapping in the mentioned higher energy state. The relative intensities of both emission bands suggest that the energy barrier from the energetically higher triplet state to the lower one increases from iodide over bromide to chloride. The low thermal energy at 10 K is insufficient to overcome this energy barrier, so that exclusively the high energy emission is observed for all the three complexes **Cu_4X_4(6-Me)$_2$**. The presented descriptions are summarized in a simplified qualitative Jablonski diagram (Figure 6).

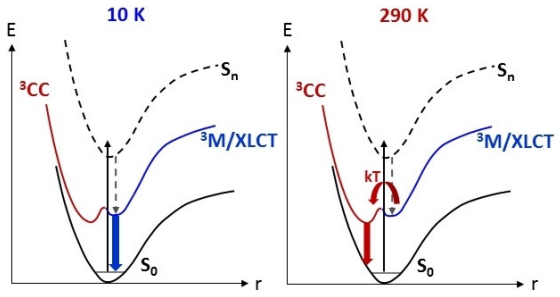

Figure 6. Qualitative energy diagram of the complexes **Cu_4X_4(6-Me)$_2$**, where the blue ^{3}M/XLCT emission at 10 K (left) and the red ^{3}CC emission at 290 K (right) are represented.

In the next step, further evaluations were performed to get a rough estimation of the mentioned energy barriers from the experimental data. The relative luminescence intensities were considered and the obtained trend for the barriers is in accordance with the suggestions elucidated above. The graphical analysis is described in more detail in the Supporting Information (Figure S32).

To gain a deeper insight into the thermochromism, the structures of the first excited triplet state (T_1) were determined for all four complexes with TDDFT. For the complexes with 6-MePyrPhos bridging ligands, two T_1 structures termed as open and closed butterfly (Figure 3) were found, while for **Cu_4I_4(4-Me)$_2$** only the closed butterfly structure was found. The closed butterfly is more stable by 22.3 kJ mol^{-1} and 9.3 kJ mol^{-1} for **Cu_4I_4(6-Me)$_2$** and **Cu_4Br_4(6-Me)$_2$**, respectively. At the same time, **Cu_4Cl_4(6-Me)$_2$** shows different behavior. The open butterfly structure is, in comparison, stabilized by 2.6 kJ mol^{-1}, which underlines the differing observation shown in Figure 5 with the open butterfly complex being already predominantly occupied at higher temperatures. Using TDDFT under consideration of the optimized T_1 structures only ^{3}M/XLCT transitions at around 735 nm (Table S3) were found when calculating the transition density of the lowest triplet excitation of the T_1 open butterfly structures (Figure S14), while the energetically favored closed butterfly structures showed exclusively ^{3}CC transitions between 800 nm and 900 nm (Figure S15 and Table S3). These findings suggest that the emission from the closed butterfly structure can be assigned to the low energy band observed at high temperature, while the blue emission band at low temperatures corresponds to the open butterfly structure as the emissive state. This behavior results from the fact that the barrier between the two structures cannot be overcome anymore, which is in agreement with the previously discussed experimental results. The lowest triplet excitations were shifted around 780 nm and 590 nm using evGW/cBSE-CAM-B3LYP (Table S3), improving the agreement with the experiment even further.

As already mentioned, the relative intensities in the temperature-dependent luminescence spectra (Figure 5) suggest increasing barriers between the two emissive states by going from **Cu_4I_4(6-Me)$_2$** over **Cu_4Br_4(6-Me)$_2$** to **Cu_4Cl_4(6-Me)$_2$**. To obtain rough estimates of the theoretical barrier heights the reaction paths between the open and closed butterfly structures were computed with TDDFT. The calculated trend is in good agreement with the experimentally observed relative emission intensities since the theoretical estimates are 2140 cm^{-1} (25.6 kJ mol^{-1}), 2339 cm^{-1} (28.7 kJ mol^{-1}) and 4656 cm^{-1} (55.7 kJ mol^{-1}) for **Cu_4I_4(6-Me)$_2$**, **Cu_4Br_4(6-Me)$_2$** and **Cu_4Cl_4(6-Me)$_2$**, respectively. The barrier heights correlate well with the energy differences between the open and closed butterfly structures, in accordance with the Bell–Evans–Polanyi principle.[40,41] A deeper understanding of the barrier heights was obtained by computing the transition densities of the lowest triplet excitation along the reaction paths. Each path was generated with 14 structures including the open and closed butterfly structures, so 12 additional structures in total. Starting from the open butterfly structure the lowest triplet excitation shows clear ^{3}M/XLCT character (Figures 7 and S14) as discussed previously, while the guess structure highest in energy has mixed ^{3}M/XLCT and ^{3}CC character. This guess structure is the 5th for **Cu_4I_4(6-Me)$_2$**, 6th for **Cu_4Br_4(6-Me)$_2$** and 7th for **Cu_4Cl_4(6-Me)$_2$** (Figures 7 and S16). This correlates well with the barrier heights as **Cu_4I_4(6-Me)$_2$** with the lowest barrier height has the earliest maximum along the reaction path, while **Cu_4Cl_4(6-Me)$_2$** with the highest barrier has the latest maximum and **Cu_4Br_4(6-Me)$_2$** is in between, in accord with Hammond's postulate.[41,42]

The presented assignment of the dual emission to the luminescent ^{3}CC and ^{3}M/XLCT states agrees with the thermochromism of similar tetranuclear copper halide clusters described in earlier reports.[10,15–19,22,23] The literature-known initial population of the ^{3}M/XLCT state followed by a thermal population of the energetically lower ^{3}CC state (after overcoming an energy barrier) is confirmed here for the systems **Cu_4X_4(6-Me)$_2$** by combining luminescence measurements at variable temperature with high-level quantum chemical calculations.

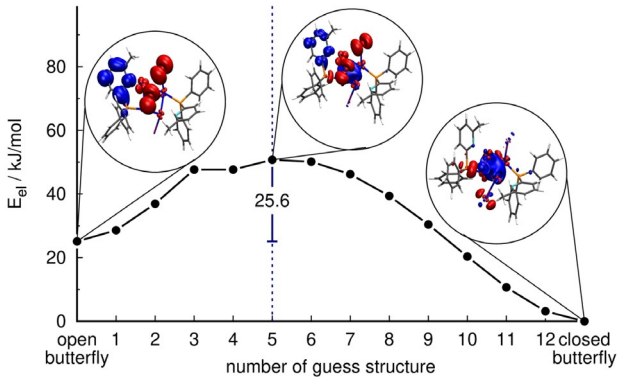

Figure 7. Illustration of the reaction path between the open and closed butterfly structures and transition densities of the lowest triplet excitation of **Cu_4I_4(6-Me)$_2$** at the open butterfly structure, the guess structure highest in energy and the closed butterfly T_1 structure.

Luminescence of solutions and neat powders

The emission spectra of the four presented complexes in ethanol EtOH are in good agreement with the KBr data and are depicted in Figure 8. It is important to mention that the dual emission of **Cu_4Br_4(6-Me)$_2$** at room temperature is clearly visible in EtOH solution with a main band at 605 nm and a very pronounced shoulder at about 480 nm. The emission pattern is preserved over 48 h so that this shoulder should not result from degradation in EtOH solution (Figure S38). The corresponding excited state lifetimes were determined to 25 μs and 30 μs for both emission features, which confirms the dual phosphorescence observed in the KBr matrix. The chloride complex shows a luminescence maximum at 491 nm with a redshifted tail up to 750 nm, which may result from a second emissive state. All the lifetimes in EtOH are equal or higher to 8.5 μs (Tables S7–S9) and are assigned to phosphorescence. At this point, it should be mentioned that no reliable TCSPC measurements could be performed in EtOH for the complex **Cu_4Cl_4(6-Me)$_2$** due to poor stability.

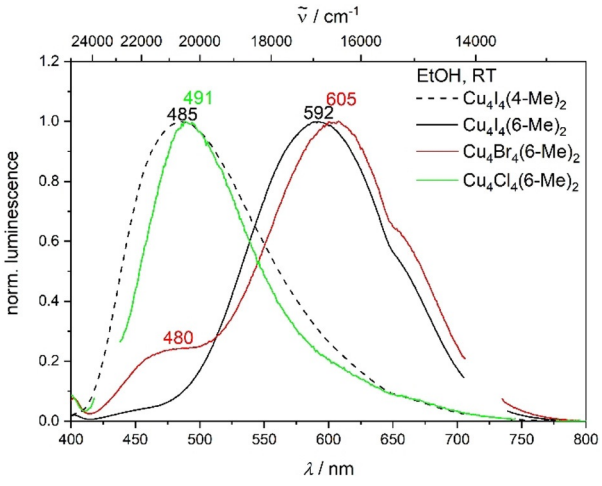

Figure 8. Emission spectra in EtOH of **Cu_4I_4(4-Me)$_2$** (λ_{ex} = 340 nm), **Cu_4I_4(6-Me)$_2$** (λ_{ex} = 360 nm), **Cu_4Br_4(6-Me)$_2$** (λ_{ex} = 360 nm) and **Cu_4Cl_4(6-Me)$_2$** (λ_{em} = 380 nm) recorded at 290 K.

Similar emission spectra were obtained of neat powders of the four samples (Figure S33). The lifetimes of 8.6 μs–35.3 μs at the emission maximum are all assigned to phosphorescence, the longest lifetime being reached for the bromide system **Cu_4Br_4(6-Me)$_2$** (Table S11). The luminescence quantum yields were determined for the powder samples, where an interesting trend was observed for the complexes with 6-MePyrPhos bridging ligands. A very high quantum yield of 93% is reached for the iodide containing complex **Cu_4I_4(6-Me)$_2$**, while the related bromide and chloride systems show values of 65% and 33%, respectively. The very high quantum yield of 93% for **Cu_4I_4(6-Me)$_2$** is known from the related binuclear complexes with a butterfly-shaped Cu_2I_2 core and phosphine ligands.[2–5] The system **Cu_4I_4(4-Me)$_2$** with 4-MePyrPhos bridging ligands shows a lower quantum yield of 58% (Table S11).

Additionally, the four systems were analyzed with respect to luminescence mechanochromism by recording luminescence spectra of neat powders before and after applying a pressure of 0.75 GPa (Figures S34–S37). Pressure induces a slight redshift of the emission maximum of **Cu_4I_4(4-Me)$_2$** by 4 nm and a small increase of the low energy emission band relative to the dominating blue emission in the case of **Cu_4Cl_4(6-Me)$_2$**. The systems **Cu_4I_4(6-Me)$_2$** and **Cu_4Br_4(6-Me)$_2$** show no mechanochromic effect. The mechanochromism with an impact of hydrostatic pressure on the luminescence properties is known from related Cu_4I_4 clusters and is mainly explained by a shortening of the Cu–Cu bond lengths in the clusters according to literature, which is however beyond the focus of this work.[10,25,43]

The emission spectra in CH_2Cl_2 strongly differ from the luminescence in the solid state and EtOH solution (Figure S39). The main emission band of the complex **Cu_4I_4(4-Me)$_2$** is redshifted to 680 nm, with a shoulder at 540 nm. A lifetime of 2.3 μs −3.6 μs was measured at 680 nm by TCSPC, depending on the excitation wavelength (Table S7). This is a clear indication for phosphorescence, whereas the lifetime at 540 nm is situated in the sub-microsecond region. Hence, the mentioned shoulder may be assigned to exciplex formation.

The described redshift of the luminescence of **Cu_4I_4(4-Me)$_2$** in CH_2Cl_2 is not observed for the system **Cu_4I_4(6-Me)$_2$** with almost identical spectra independent of the medium (emission maxima at 593 nm, 592 nm and 590 nm in KBr, EtOH and CH_2Cl_2, respectively) and throughout lifetimes on the microsecond time scale (Table S8). Hence, the emissive triplet structures have to be very similar in CH_2Cl_2 and EtOH solution. However, the bromide and chloride analogues also show the strong redshift described above for **Cu_4I_4(4-Me)$_2$**, with the main emission band being split into two close-lying emission peaks separated by 730 cm^{-1} for **Cu_4Br_4(6-Me)$_2$** and 815 cm^{-1} for **Cu_4Cl_4(6-Me)$_2$** (Figure S39). These features may be assigned to a vibrational progression, which is consistent with the almost identical time constants obtained for both emission maxima, that are again in accordance with phosphorescence (Tables S9 and S10). Additionally, the bromide containing system shows a shoulder at 544 nm, whose relative intensity decreases over time, so that this feature cannot be assigned to the proper complex (Figure S40).

In the context of the luminescence studies in solution, it is important to mention that the ground state FTIR spectrum of **Cu_4Cl_4(6-Me)$_2$** in CD_2Cl_2 solution is almost identical to the solid state IR spectrum (Figure S41), confirming the presence of the intact species also in liquid solution. At the same time, the similar luminescence data in KBr, neat powder and EtOH as well as their lifetimes confirm the stability of the complexes in solution (Tables S7–S10). Additionally, it should be mentioned that clean NMR spectra were obtained in [D_6]DMSO solution (Figures S1–S6).

Furthermore, (unrestricted) DFT structure optimizations of the S_0 and the T_1 states via the COSMO model were conducted in CH_2Cl_2 and EtOH. The most important result with respect to the relative energies is that the closed butterfly T_1 structures are at least 50 kJ mol^{-1} lower in energy than the corresponding C_i symmetric T_1 structures (Table S17). The relative trends found for the energy gaps between the S_0 and closed butterfly T_1 structures agree with the observed emission spectra. The energy differences in CH_2Cl_2 are slightly smaller for **Cu_4I_4(4-Me)$_2$**, **Cu_4Br_4(6-Me)$_2$** and **Cu_4Cl_4(6-Me)$_2$** compared to EtOH by up to 3.1 kJ mol^{-1}. At the same time, the S_0–T_1 energy gap is almost completely unaffected by the solvent for **Cu_4I_4(6-Me)$_2$**, in accordance with the emission spectra. This is a further indication that only one triplet structure (closed butterfly) is present in solution.

Temperature-dependent step-scan FTIR investigations in the solid state

Step-scan FTIR investigations were performed in the KBr matrix to elucidate the structural changes involved in the excited state thermochromism of the presented systems with 6-MePyrPhos bridging ligands. For this purpose, we performed step-scan FTIR experiments on the series **Cu_4X_4(6-Me)$_2$** and considered the related system **Cu_4I_4(4-Me)$_2$** without thermochromism as a reference. Considering the series **Cu_4X_4(6-Me)$_2$**, particularly the compound **Cu_4I_4(6-Me)$_2$** is an ideal benchmark to probe two different electronically excited states by step-scan FTIR spectroscopy at 20 K and 290 K, as the luminescence investigations clearly showed a completely inversed population of the long-lived electronically excited states by cooling down the sample from 290 K to 20 K. The presented IR studies are supported by theoretical calculations to access profound structural information, especially for the electronically excited states.

The calculated ground state IR spectra of the C_i symmetric and closed butterfly-shaped isomers of **Cu_4I_4(4-Me)$_2$** are very similar and in very good agreement with the measured FTIR spectrum (Figures 9 and S42), so that a clear assignment is not possible by considering only the ground state IR absorption. The IR spectra are recorded in KBr pellets, a technique that has now also been established for transient IR spectroscopy.[1,8,9,33,44] The ground state FTIR spectra at 20 K and 290 K are very similar and do not indicate pronounced structural changes as a function of temperature (Figure S43). All the vibrations and calculated geometries of the four investigated compounds are described in detail in the Supporting Information.

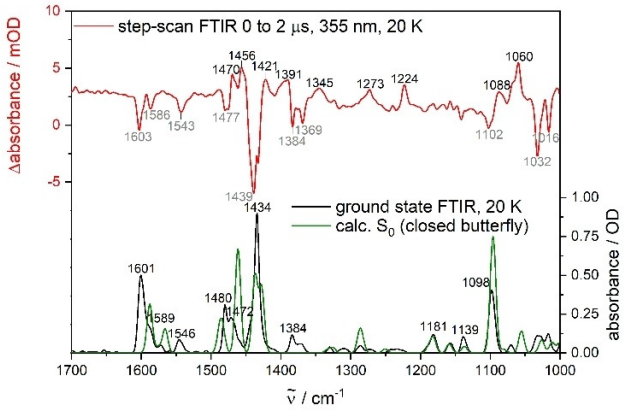

Figure 9. Step-scan FTIR spectrum 0 µs to 2 µs after excitation at λ_{ex} = 355 nm, ground state FTIR spectrum (KBr pellet, 20 K) and DFT calculated IR spectrum of **Cu_4I_4(4-Me)$_2$** (scaled by 0.975, FWHM = 8 cm^{-1}, Gaussian profile) (DFT/B3LYP-D3(BJ)/def2-TZVP).

In the time-resolved experiments, the sample was excited with a 355 nm laser pulse and a step-scan difference spectrum was recorded. The first 2 µs after laser excitation are considered in the step-scan spectrum measured at 20 K, which is shown in Figure 9. The negative bleach bands correspond to the ground state vibrations and result from the depopulation of the electronic ground state, whereas the positive bands are assigned to the populated electronically excited state(s). As the luminescence investigations clearly indicate phosphorescence from the same triplet state, independent of temperature the lowest excited triplet state T_1 should be populated. Thus, the positive bands in the step-scan spectrum should result from the lowest triplet state T_1. The T_1 structures were optimized by TDDFT under consideration of the described C_i symmetric and closed butterfly-shaped ground state geometries as input structures, followed by harmonic frequency calculations to obtain the corresponding IR spectra of the excited triplet states. For a good comparison of the calculated T_1 spectra with the measured step-scan spectrum, the experimental pure excited state spectra were generated by addition of 3% of the ground state spectrum to the step-scan difference spectrum. Hence, the negative bleach bands are suppressed and the positive features correspond to the IR spectrum of the observed electronically excited state(s) without any contribution of the electronic ground state. In contrast to the calculated S_0 spectra, the calculated T_1 spectra of the C_i symmetric and closed butterfly-shaped structures show significant differences (Figure 10). The IR spectrum of the closed butterfly structure is in very good agreement with the experimental excited state spectrum at 20 K, which is not the case for the C_i isomer. The corresponding theoretical IR spectrum of this C_i structure shows strong bands at 1011, 1057, 1227, 1284, 1355 and 1527 cm^{-1}, which are not observed experimentally.

The same step-scan experiment was then performed at 290 K, the obtained difference spectrum is depicted in Figure S44. For a better comparison between the transient IR experiments at 20 K and 290 K, the pure excited state spectra were generated by addition of 3% of the corresponding

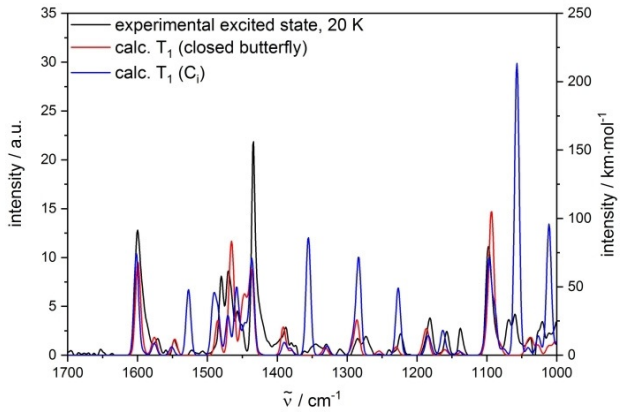

Figure 10. Experimental excited state spectrum at 20 K (addition of 3 % of the ground state spectrum to the step-scan difference spectrum) and calculated T_1 spectra (closed butterfly and C_i structures) of **Cu_4I_4(4-Me)$_2$** (scaled by 0.975, FWHM = 8 cm^{-1}, Gaussian profile) (TDDFT/B3LYP-D3(BJ)/def2-TZVP).

ground state spectrum to the step-scan spectrum to suppress the negative bleach bands. The obtained excited state spectra are very similar (Figure S45) so that they can be assigned to the same excited triplet state. The small discrepancies (e.g. slightly blueshifted bands and weak shoulder at 1457 cm^{-1} at 20 K) should result from small structural changes due to the higher thermal energy at 290 K and not from separate electronically excited states. Thus, the same triplet state is also observed at 290 K and is in very good agreement with the corresponding theoretical spectrum (Figure S46). At this point, it should be mentioned that the calculated IR spectra of the lowest electronically excited states S_1 and T_1 are almost identical (especially for the closed butterfly structure, Figure S47) so that the S_1 state cannot be directly excluded from the discussion from this point of view. However, the time-resolved luminescence measurements with a long decay time of 5 µs already at 290 K and static emission spectra without any redshift of the emission at low temperature (typical for TADF) allow an assignment to phosphorescence. For a deeper interpretation, it has to be considered that, according to theory, only the closed butterfly structure shows the measured almost temperature-independent low energy cluster-centered phosphorescence (Figure S17, Table S3). Hence, the observed long-lived electronically excited state can be assigned unambiguously to the closed butterfly-shaped T_1 state by combining time-resolved FTIR and luminescence spectroscopy as well as theory. In this context, it is probable that the complex molecules in the powder sample of **Cu_4I_4(4-Me)$_2$** are of closed butterfly geometry also in the electronic ground state, as huge structural changes must instead occur upon UV excitation and population of the studied triplet state. The C_i symmetry may be favored in the crystal matrix due to packing effects (see the paragraph on crystallography).

In the next step, the transient FTIR investigations were extended to the complex **Cu_4I_4(6-Me)$_2$**, showing luminescence thermochromism. The position of the methyl group slightly affects the vibrational spectrum in the electronic ground state, especially between 1400 and 1600 cm^{-1} (Figure S48). As described above, two different isomers (C_i symmetric and open butterfly) were found with DFT, which have to be considered here. The calculated S_0 spectra of both isomers of **Cu_4I_4(6-Me)$_2$** are almost identical and in very good agreement with the experiment, so that no clear assignment of one isomer to the investigated powder sample is possible from this point of view (Figure S50). Additionally, the FTIR ground state spectrum is barely influenced by temperature (Figure S49). Transient FTIR spectroscopy was then performed at 20 K and 290 K, where significant discrepancies were observed between the step-scan difference spectra (Figures 11, S51 and S52). For a better comparison between the step-scan results at 20 K and 290 K the pure excited state spectra were generated by addition of 1 % of the corresponding FTIR ground state spectrum to the step-scan difference spectrum (Figures 12 and S53). Interestingly, three intense bands are observed at 1402, 1267 and 1039 cm^{-1} in the excited state spectrum at 20 K, which are significantly

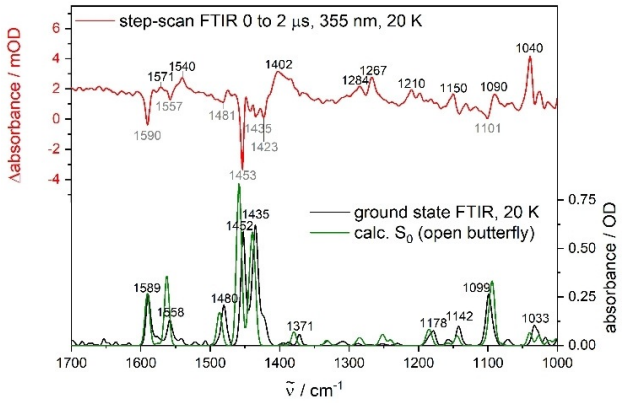

Figure 11. Step-scan FTIR spectrum 0 µs to 2 µs after excitation at λ_{ex} = 355 nm, ground state FTIR spectrum (KBr pellet, 20 K) and DFT calculated S_0 (C_1 symmetry spectrum of **Cu_4I_4(6-Me)$_2$** (scaled by 0.975, FWHM = 8 cm^{-1}, Gaussian profile) (DFT/B3LYP-D3(BJ)/def2-TZVP).

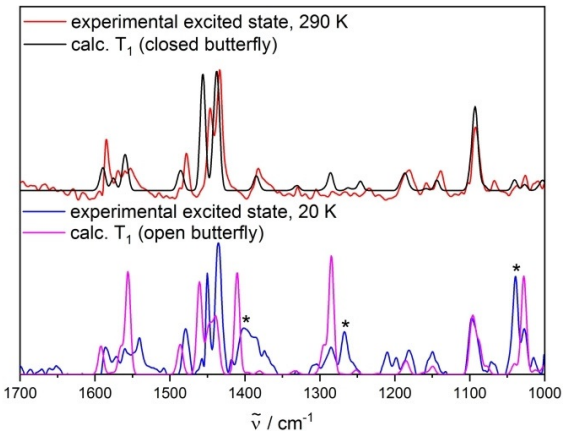

Figure 12. Experimental excited state spectra at 20 K and 290 K (generated by addition of 1 %of the ground state spectrum to the step-scan spectrum), as well as calculated T_1 spectra (open and closed butterfly structures) of **Cu_4I_4(6-Me)$_2$** (scaled by 0.975, FWHM = 8 cm^{-1}, Gaussian profile) (TDDFT/B3LYP-D3(BJ)/def2-TZVP).

redshifted (from 1402 cm^{-1} to 1382 cm^{-1}), much weaker (for 1039 cm^{-1}) or even completely absent at 290 K (for 1267 cm^{-1}) (asterisks in Figures 12 and S53).

In Figure 12, the theoretical excited triplet IR spectra of the found open and closed butterfly minima structures (see above) are compared with the measured excited state spectra. At 20 K, the new excited state-specific experimental bands highlighted with asterisks in Figure 12 are only described by the calculated spectrum of the open butterfly isomer. These intense peaks are assigned to delocalized vibrational modes, which are described in more detail in the Supporting Information (Table S13). Simultaneously, the observed effects at 290 K (e.g. redshift of about 20 cm^{-1}) can only be explained by considering the closed butterfly isomer (Figure 12). The same assignment is obtained by comparing the measured step-scan difference spectra directly with the corresponding theoretical difference spectra (T_1–S_0) (Figures S54 and S55).

At 20 K and thus for the open butterfly isomer, the underlying electronic transition corresponds to a ^{3}M/XLCT charge transfer from the cluster core of **Cu_4I_4(6-Me)$_2$** to one of the 6-MePyrPhos ligands (Figures S14 and S79). This charge transfer significantly affects the bond lengths in one of the bridging ligands and also leads to structural changes in the cluster core (Table S26). Hence, the observation of this electronically excited triplet state in the step-scan experiment at 20 K is in perfect agreement with the intense blue emission seen in the luminescence spectra at low temperature. Simultaneously, the assignment of the closed butterfly isomer to the excited state IR spectrum measured at 290 K is clearly following the observed ^{3}CC low energy emission at higher thermal energy. In this case, the electronic transition is limited to the cluster core, so that the structural changes in the bridging ligands are smaller (Table S27). This also explains that the features observed in the excited state at 290 K are closer to those in the ground state IR spectrum, whereas pronounced new bands appear at 20 K upon UV excitation. Nevertheless, it has to be mentioned that the closed butterfly core structure of the ^{3}CC state strongly deviates from the open butterfly Cu_4I_4 cluster geometries of the S_0 and ^{3}M/XLCT states, which are quite similar. This behavior is sketched in the simplified energy Scheme in Figure 6 by the relative positioning of the potential curves along the abscissa of the respective states. The analogous cluster geometries of the S_0 and ^{3}M/XLCT states and hence the almost nested energy potentials are responsible for the described kinetic trapping at low temperatures.

It should be mentioned that the theoretical T_1 and S_1 IR spectra are again very similar (Figure S56), but the long excited state lifetimes of several microseconds (see paragraph on luminescence investigations) clearly disagree with a direct fluorescence from the S_1 state which should be in the region of nanoseconds.

As the bromide and chloride analogues of **Cu_4I_4(6-Me)$_2$** also showed the thermochromism in the temperature-dependent luminescence investigations, step-scan measurements were performed on these systems for comparison.

First of all, it should be mentioned that the ground state FTIR spectra are hardly influenced by the halide exchange, which is very well reproduced by the theoretical calculations (Figure S57). The calculated S_0 spectra of the found C_i symmetric and open butterfly minimum structures are very similar also for **Cu_4Br_4(6-Me)$_2$** and **Cu_4Cl_4(6-Me)$_2$** (Figures S58 and S59).

At first sight, the step-scan difference spectra at 20 K and 290 K of the bromide and chloride systems show strong similarities compared to those obtained for **Cu_4I_4(6-Me)$_2$** (Figures S60–S63). For a better direct comparison, the experimental excited state spectra at both temperatures were generated and depicted in Figure 13 (Figures S68 and S69). Indeed, all the strong new bands observed at 20 K for the iodide complex with thermochromic effects are also observed for the bromide and chloride analogues (see asterisks in Figure 13). According to the calculated excited triplet frequencies, the time-resolved spectra at 290 K and 20 K are assigned to the closed and open butterfly structures, respectively (Figures S64–S67). However, it should be noticed that the excited state-specific bands of **Cu_4Cl_4(6-Me)$_2$** at 20 K (see asterisks in Figure 13) are weak relative to the other peaks, whereas these features are much stronger for the iodide and bromide complexes. This observation may explain the absence of the mentioned bands at 290 K in the case of **Cu_4Cl_4(6-Me)$_2$**, even if the luminescence spectra indicate a significant population of the open butterfly triplet state.

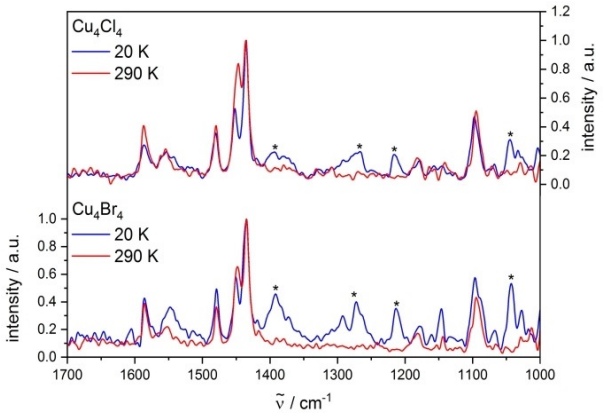

Figure 13. Experimental excited state spectra at 20 K and 290 K (generated by addition of 1% of the ground state spectrum to the step-scan spectrum) of **Cu_4Br_4(6-Me)$_2$** (bottom) and **Cu_4Cl_4(6-Me)$_2$** (top).

Finally, it can be concluded that the structural changes involved in the thermochromism are mainly navigated by the position of the methyl group on the bridging ligand. At the same time, the halide exchange has only a rather small influence on the structures of the excited triplet states (see Supporting Information for structural parameters), but tunes the energy barrier between these emissive ^{3}CC and ^{3}M/XLCT states (cf. energy barriers).

Conclusions

In this work, we have presented the synthesis and a thorough multi-spectroscopic characterization of a series of tetranuclear

Cu^{I} complexes with halide containing Cu_4X_4 core units (X = iodide, bromide and chloride) and 2-(diphenylphosphino)pyridine (PyrPhos) bridging ligands with a methyl substituent in *para* (4-Me) or *ortho* (6-Me) position. The experimental data were interpreted in combination with high-level quantum chemical calculations.

Interestingly, all three complexes with 6-MePyrPhos bridging ligands showed a remarkable luminescence thermochromism with dual phosphorescence from a metal/halide-to-ligand charge transfer (^{3}M/XLCT) and a cluster-centered (^{3}CC) triplet state. The temperature-dependent luminescence investigations revealed that both emissive triplet states are separated by an energy barrier, whose magnitude is significantly influenced by the halide exchange and has a massive impact on the thermochromism. The luminophores showed temperature-dependent emission spectra which cover the whole visible region. The bridging ligands also have a very big impact on the photophysical properties; in contrast to the complexes with 6-MePyrPhos bridging ligands, the complex **Cu_4I_4(4-Me)$_2$** with a methyl group in the *para* position of the bridging ligand did not show this thermochromism.

A central aspect of this work is the structural characterization of the long-lived electronically excited states involved in the observed luminescence behavior. Time-resolved (transient) step-scan FTIR spectroscopy in combination with DFT calculations turned out to be an ideal tool to identify the excited structures of the solid samples of **Cu_4I_4(4-Me)$_2$** as well as the series **Cu_4X_4(6-Me)$_2$** (X = iodide, bromide, chloride). As the relative population of the triplet states can be fully reversed in the case of **Cu_4I_4(6-Me)$_2$** by cooling down the sample from 290 K to 20 K, this complex was an ideal benchmark system to analyze two different electronically excited states of a single complex by transient IR spectroscopy for the first time. The combination of a variety of spectroscopic methods including transient IR spectroscopy offers a unique tool to identify relative energies *and* (T-dependent) structures of electronically excited states for a variety of efficient luminophores.

Experimental Section

Experimental details

Single crystal X-ray diffraction data were collected on an STOE STADI VARI diffractometer with monochromated Ga Kα (λ = 1.34143 Å) radiation at low temperature. Using Olex2[45] the structures were solved with the ShelXT[46] structure solution program using Intrinsic Phasing and refined with the ShelX[47] refinement package using Least Squares minimization. Refinement was performed with anisotropic temperature factors for all non-hydrogen atoms; hydrogen atoms were calculated on idealized positions.

UV/Vis absorbance experiments were performed with a Lambda 900 UV/Vis spectrometer in CH_2Cl_2 solutions that were measured in 10 mm path length quartz cells at 25 °C. The solutions were prepared using the common Schlenk technique with concentrations in the range of 2×10^{-5} M The spectra were recorded relative to the pure solvent.

For the preparation of KBr pellets, the copper complexes (1.6 mg–1.8 mg) were mixed with dry KBr (200 mg, stored in a compartment dryer at 80 °C, purchased from Merck) and ground to a homogenous mixture. This mixture was filled in an evacuable pellet die with a diameter of 13 mm and sintered at a pressure of 0.75 GPa at room temperature.

Neat films were prepared by spraying a fine suspension of the compound in CH_2Cl_2 on a CaF_2 substrate (13 mm diameter, 1 mm thick), followed by evaporation of the solvent.

Steady-state luminescence measurements on KBr pellets, neat films and neat powders were performed on a Horiba Jobin Yvon FluoroMax-2 spectrometer. Temperature-dependent measurements were performed using a closed-cycle helium cryostat (ARS Model DE-202A) to cool down the sample to 20 K. The cryo cooler was equipped with a pellet holder (copper) and CaF_2 windows. A 150 W xenon lamp was used for sample excitation and detection was realized with a R928 photomultiplier detector. The spectral selection was achieved with single grating monochromators in the excitation and emission paths, respectively. Luminescence lifetimes were determined by TCSPC (Time-correlated single-photon counting) using a DeltaFlex (Horiba Scientific) spectrometer. Excitation sources: NanoLED 390 (wavelength: 389 nm, pulse duration: 1.3 ns), NanoLED 350 (wavelength: 345 nm, pulse duration: $<$1 ns). Long-wave pass filters (cutoff at 436 nm; 475 nm; 500 nm; 540 nm or 600 nm) were set between sample and emission monochromator to suppress the influence of scattered excitation light. Decay curves were analyzed by multiexponential fits with the software ORIGIN®.

Static emission spectra in solution were recorded using a Fluorolog 3–22 τ (Horiba Jobin–Yvon) fluorescence spectrometer. Spectroscopic grade solvents were purchased from Merck and degassed by multiple pump freeze cycles before usage. The solutions were prepared using the common Schlenk technique with concentrations in the range of 2×10^{-5} M and measured in 1 cm *x* 1 cm quartz cuvettes. Lifetimes were determined by TCSPC using the same setup as used for the KBr pellets. Excitation sources: NanoLED 390 (wavelength: 389 nm, pulse duration: 1.3 ns), NanoLED 350 (wavelength: 345 nm, pulse duration: $<$1 ns), NanoLED 320 (wavelength: 313 nm, pulse duration: $<$1 ns). The instrumental response function (IRF) of 125 ps (FWHM) was collected by the use of LUDOX®. Decay curves were analyzed by mono-/multiexponential fits with the software ORIGIN®.

Time-resolved luminescence experiments of neat powders were performed by a Horiba Scientific, model FluoroMax-4 equipped with a 150 W Xenon-Arc lamp, excitation- and emission monochromators and a Hamamatsu R928 photomultiplier and a time-correlated single-photon counting option. Excited state lifetimes were determined employing the same system using the TCSPC method with FM-2013 equipment and a Horiba Yvon TCSPC hub. Excitation sources: NanoLED 370 (wavelength: 371 nm, pulse duration: 1.1 ns), NanoLED 290 (wavelength: 294 nm, pulse duration: $<$1 ns), SpectraLED 310 (wavelength: 314 nm), SpectraLED 355 (wavelength: 355 nm). Data analysis (exponential fit) was done using the software suite DataStation and DAS6 analysis software. The fit is specified using the chi-squared-test. For the photoluminescence quantum yield (PLQY) measurements an Absolute PLQY measurement C9920-03G system (Hamamatsu Photonics) was used. Quantum yields and CIE coordinates were determined using the software U6039-05 version 3.6.0. Quantum yields Φ are given in % and CIE coordinates as *x*, *y* values. The PLQYs were measured with an integrating sphere set up of the powder of the Cu^{I} complexes with an excitation wavelength of 350 nm. The yield was calculated using the following equation, wherein n_{photon} denotes the photon count and *Int.* the intensity [Eq (1)].

$$\Phi_{PL} = \frac{n_{photon,\ emitted}}{n_{photon,\ absorbed}} = \frac{\int \frac{\lambda}{hc}\left[Int^{sample}_{emitted}(\lambda) - Int^{sample}_{absorbed}(\lambda)\right]d\lambda}{\int \frac{\lambda}{hc}\left[Int^{reference}_{emitted}(\lambda) - Int^{reference}_{absorbed}(\lambda)\right]d\lambda} \quad (1)$$

The general experimental setup for step-scan measurements has been described in detail in earlier works so that only a brief description of the general setup is given here.[9,32]

All the time-resolved FTIR experiments were performed with the FTIR spectrometer Bruker Vertex 80v, operated in the step-scan mode. A liquid-nitrogen-cooled mercury cadmium telluride (MCT) detector (Kolmar Tech., Model KV100-1-B-7/190) with a rise time of 25 ns, connected to a fast preamplifier and a 14-bit transient recorder board (Spectrum Germany, M3I4142, 400 MS s^{-1}), was used for signal detection and processing. The laser setup used for the measurements includes a Q-switched Nd:YAG laser (Innolas Spit-Light Evo I) generating pulses with a bandwidth of about 6 ns at a repetition rate of 100 Hz. The third harmonic (355 nm) of the Nd:YAG laser was used directly for sample excitation. The UV pump beam was attenuated to about 2.0 mJ per shot at a diameter of 9 mm. The beam was directed onto the sample and adjusted to have a maximal overlap with the IR beam of the spectrometer. The sample chamber was equipped with anti-reflection-coated germanium filters to prevent the entrance of laser radiation into the detector and interferometer compartments. The KBr pellets were prepared as described above and cryogenically cooled (20 K or 290 K at the pellet) with the cryostat presented earlier. The temporal resolution of the 14-bit transient recorder board was set to 10 ns for **Cu_4I_4(4-Me)$_2$** or 20 ns for the series **Cu_4X_4(6-Me)$_2$**. The step-scan measurement was started 1 μs or 2 μs before the laser pulse reached the sample. The time where the laser pulse reached the sample was set as zero point in all spectra. The time delay between the start of the experiment and the laser pulse was controlled with a *Stanford Research Systems* DG535 delay generator. The spectral region was limited by under-sampling to 0–1975 cm^{-1} or 988–1975 cm^{-1} with a spectral resolution of 4 cm^{-1} resulting in 1110/555 interferogram points, respectively. An IR broadband filter (850–1750 cm^{-1}) and CaF_2 windows (no IR transmission $<1000\ cm^{-1}$) prevented problems when performing a Fourier transformation (i.e. no IR intensity outside the measured region should be observed). FTIR ground state spectra were recorded systematically to check if there is no sample degradation.

Theoretical calculations

The crystal structures and geometries generated by chemical intuition were used as input structures. Geometry optimizations were performed with the Berny algorithm of Gaussian 09[48] by using energies and gradients computed by Turbomole 7.4.[49,50] All calculations were performed with the DFT functional B3LYP with dispersion correction (no three-body interaction) (D3(BJ))[51] as implemented in Turbomole using the resolution of identity (RI) approximation and the def2-TZVP (def2-ecp for iodide) basis set. The energetically lowest excited states were optimized by TDDFT with the same functional and basis set as in the ground state. All the indicated relative energies are corrected by the zero-point vibrational energy. Absorption spectra were simulated by using TDDFT and calculating 100 electronic excitations in the singlet manifold. Solvent effects were modulated by using the conductor-like screening model (COSMO) (cf. chapter on luminescence investigations in solution). Obtained geometries were tested for minimum structures by application of frequency calculations, for which no imaginary modes were found. Only the open butterfly structure of **Cu_4Cl_4(6-Me)$_2$** showed a negative frequency of $-7.4\ cm^{-1}$. The vibrational frequencies are scaled by a factor of 0.975, which is typical for the chosen method and basis set, to minimize the differences between the experimental and calculated frequencies. A gaussian convolution with a full-width at half-maximum of 8 cm^{-1} was applied to the calculated vibrational transitions. Turbomole 7.4[49,50] was used for computing the UV/Vis spectra with TDDFT CAM-B3LYP[35] and evGW/cBSE[37,38] using contour deformation[52] and CAM-B3LYP (CD-evGW(10)cBSE-CAM-B3LYP). For convolution Gaussian broadening with a full-width at half maximum of 2500 cm^{-1} was used. The 12 additional structures of the reaction paths were obtained by the initial guess reaction path of the WOELFLING program.[53]

Synthesis

For the performance of all reactions in this study, the general Schlenk conditions were applied. Details on the purchase of solvents and compounds are given in the Supporting Information.

The bridging phosphine ligands 4-methyl-2-(diphenylphosphino)-pyridine and 6-methyl-2-(diphenylphosphino)pyridine were synthesized according to the literature procedure with elemental lithium and chlorodiphenyl-phosphine in dry tetrahydrofuran (SPS system, degassed with argon for 20 min after tapping). The analytical results of the colorless powders were in accordance with the literature protocols.[54]

The tetranuclear complexes were synthesized according to a general procedure. A 20 mL crimp vial was charged with the NP-bridging ligand (3.00 mmol, 2.00 equiv.), the corresponding Cu^{I} halide (6.00 mmol, 4.00 equiv.) and 15 mL of dry CH_2Cl_2. The resulting suspension was degassed with argon for five minutes and was stirred overnight (12 h) at ambient temperature. The reaction mixture was added dropwise to an excess of *n*-pentane (300 mL). The precipitate was filtered off and was washed with small portions of *n*-pentane and diethyl ether. The powders were dried in vacuo. Crystals were obtained of the filtrate by slow evaporation of the solvent in the fume hood or by the layering approach with CH_2Cl_2 and *n*-pentane in small vials.

Further details on the synthesis of the specific complexes are given in the Supporting Information. The details on the chemical synthesis and original analytical data were added to the repository Chemotion (www.chemotion.net/home). The corresponding codes are given in brackets. Cu_4I_4(4-Me)$_2$ (CRR 9266), Cu_4I_4(6-Me)$_2$ (CRR 11659), Cu_4Br_4(6-Me)$_2$ (CRR 9926), Cu_4Cl_4(6-Me)2 (CRR 9935).

Acknowledgements

We gratefully acknowledge the support by the Deutsche Forschungsgemeinschaft (DFG) SFB/TRR 88 "3 MET" (Projects C2, C4 and T1) and the support of the research center OPTIMAS. We also thank the Karlsruhe School of Optics and Photonics (KSOP) for their financial support. Additionally, the DFG under Germany's Excellence Strategy-3DMM2O—EXC-2082/1–390761711 is acknowledged. And we acknowledge the previous work of Daniel Zink who described the complex **Cu_4I_4(6-Me)$_2$** already in his doctoral thesis. Open access funding enabled and organized by Projekt DEAL.

Keywords: Cu^{I} complexes · FTIR spectroscopy · luminescence · theoretical calculations · X-ray diffraction

[1] J. M. Busch, D. M. Zink, P. Di Martino-Fumo, F. R. Rehak, P. Boden, S. Steiger, O. Fuhr, M. Nieger, W. Klopper, M. Gerhards, S. Bräse, *Dalton Trans.* **2019**, *48*, 15687.
[2] D. Volz, D. M. Zink, T. Bocksrocker, J. Friedrichs, M. Nieger, T. Baumann, U. Lemmer, S. Bräse, *Chem. Mater.* **2013**, *25*, 3414.
[3] D. M. Zink, D. Volz, T. Baumann, M. Mydlak, H. Flügge, J. Friedrichs, M. Nieger, S. Bräse, *Chem. Mater.* **2013**, *25*, 4471.
[4] D. M. Zink, M. Bächle, T. Baumann, M. Nieger, M. Kühn, C. Wang, W. Klopper, U. Monkowius, T. Hofbeck, H. Yersin, S. Bräse, *Inorg. Chem.* **2013**, *52*, 2292.
[5] D. Volz, M. Wallesch, S. L. Grage, J. Göttlicher, R. Steininger, D. Batchelor, T. Vitova, A. S. Ulrich, C. Heske, L. Weinhardt, T. Baumann, S. Bräse, *Inorg. Chem.* **2014**, *53*, 7837.
[6] a) D. Volz, Y. Chen, M. Wallesch, R. Liu, C. Fléchon, D. M. Zink, J. Friedrichs, H. Flügge, R. Steininger, J. Göttlicher, C. Heske, L. Winhardt, S. Bräse, F. So, T. Baumann, *Adv. Mater.* **2015**, *27*, 2538; b) K. Tsuge, Y. Chishina, H. Hashiguchi, Y. Sasaki, M. Kato, S. Ishizaka, N. Kitamura, *Coord. Chem. Rev.* **2016**, *306*, 636.
[7] T. Hofbeck, U. Monkowius, H. Yersin, *J. Am. Chem. Soc.* **2015**, *137*, 399.
[8] F. Bäppler, M. Zimmer, F. Dietrich, M. Grupe, M. Wallesch, D. Volz, S. Bräse, M. Gerhards, R. Diller, *Phys. Chem. Chem. Phys.* **2017**, *19*, 29438.
[9] M. Zimmer, F. Dietrich, D. Volz, S. Bräse, M. Gerhards, *ChemPhysChem* **2017**, *18*, 3023.
[10] A. Neshat, R. B. Aghakhanpour, P. Mastrorilli, S. Todisco, F. Molani, A. Wojtczak, *Polyhedron* **2018**, *154*, 217.
[11] A. Y. Baranov, A. S. Berezin, D. G. Samsonenko, A. S. Mazur, P. M. Tolstoy, V. F. Plyusnin, I. E. Kolesnikov, A. V. Artem'ev, *Dalton Trans.* **2020**, *49*, 3155.
[12] J. Zhang, C. Duan, C. Han, H. Yang, Y. Wei, H. Xu, *Adv. Mater.* **2016**, *28*, 5975.
[13] a) H. V. R. Dias, H. V. K. Diyabalanage, M. A. Rawashdeh-Omary, M. A. Franzman, M. A. Omary, *J. Am. Chem. Soc.* **2003**, *125*, 12072; b) H. V. R. Dias, H. V. K. Diyabalanage, M. G. Eldabaja, O. Elbjeirami, M. A. Rawashdeh-Omary, M. A. Omary, *J. Am. Chem. Soc.* **2005**, *127*, 7489; c) Q. Xiao, J. Zheng, M. Li, S.-Z. Zhan, J.-H. Wang, D. Li, *Inorg. Chem.* **2014**, *53*, 11604; d) A. A. Titov, O. A. Filippov, A. F. Smol'yakov, I. A. Godovikov, J. R. Shakirova, S. P. Tunik, I. S. Podkorytov, E. S. Shubina, *Inorg. Chem.* **2019**, *58*, 8645; e) J. Zheng, H. Yang, M. Xie, D. Li, *Chem. Commun.* **2019**, *55*, 7134; f) J. Zheng, Z. Lu, K. Wu, G.-H. Ning, D. Li, *Chem. Rev.* **2020**, *120*, 9675; g) L.-R. Xing, Z. Lu, M. Li, J. Zheng, D. Li, *J. Phys. Chem. Lett.* **2020**, *11*, 2067.
[14] X.-L. Chen, R. Yu, X.-Y. Wu, D. Liang, J.-H. Jia, C.-Z. Lu, *Chem. Commun.* **2016**, *52*, 6288.
[15] S. Perruchas, C. Tard, X. F. Le Goff, A. Fargues, A. Garcia, S. Kahlal, J.-Y. Saillard, T. Gacoin, J.-P. Boilot, *Inorg. Chem.* **2011**, *50*, 10682.
[16] F. de Angelis, S. Fantacci, A. Sgamellotti, E. Cariati, R. Ugo, P. C. Ford, *Inorg. Chem.* **2006**, *45*, 10576.
[17] Q. Benito, X. F. Le Goff, G. Nocton, A. Fargues, A. Garcia, A. Berhault, S. Kahlal, J.-Y. Saillard, C. Martineau, J. Trébosc, T. Gacoin, J.-P. Boilot, S. Perruchas, *Inorg. Chem.* **2015**, *54*, 4483.
[18] S. Nagaoka, Y. Ozawa, K. Toriumi, M. Abe, *Chem. Lett.* **2018**, *47*, 1101.
[19] S. Perruchas, X. F. Le Goff, S. Maron, I. Maurin, F. Guillen, A. Garcia, T. Gacoin, J.-P. Boilot, *J. Am. Chem. Soc.* **2010**, *132*, 10967.
[20] H. Kitagawa, Y. Ozawa, K. Toriumi, *Chem. Commun.* **2010**, *46*, 6302.
[21] K. Chen, J. Shearer, V. J. Catalano, *Inorg. Chem.* **2015**, *54*, 6245.
[22] A. Lapprand, M. Dutartre, N. Khiri, E. Levert, D. Fortin, Y. Rousselin, A. Soldera, S. Jugé, P. D. Harvey, *Inorg. Chem.* **2013**, *52*, 7958.
[23] Z. Liu, P. I. Djurovich, M. T. Whited, M. E. Thompson, *Inorg. Chem.* **2012**, *51*, 230.
[24] a) Y.-D. Yu, L.-B. Meng, Q.-C. Chen, G.-H. Chen, X.-C. Huang, *New J. Chem.* **2018**, *42*, 8426; b) L. Yao, G. Niu, J. Li, L. Gao, X. Luo, B. Xia, Y. Liu, P. Du, D. Li, C. Chen, Y. Zheng, Z. Xiao, J. Tang, *J. Phys. Chem. Lett.* **2020**, *11*, 1255; c) Z.-J. Lv, P.-N. Jin, Y.-H. Wang, X.-B. Wei, G. Yang, *J. Cluster Sci.* **2015**, *26*, 1389.
[25] B. Huitorel, R. Utrera-Melero, F. Massuyeau, J.-Y. Mevelec, B. Baptiste, A. Polian, T. Gacoin, C. Martineau-Corcos, S. Perruchas, *Dalton Trans.* **2019**, *48*, 7899.
[26] A. V. Artem'ev, A. Y. Baranov, M. I. Rakhmanova, S. F. Malysheva, D. G. Samsonenko, *New J. Chem.* **2020**, *44*, 6916.
[27] A. V. Shamsieva, I. E. Kolesnikov, I. D. Strelnik, T. P. Gerasimova, A. A. Kalinichev, S. A. Katsyuba, E. I. Musina, E. Lähderanta, A. A. Karasik, O. G. Sinyashin, *J. Phys. Chem. C* **2019**, *123*, 25863.
[28] E. I. Musina, A. V. Shamsieva, I. D. Strelnik, T. P. Gerasimova, D. B. Krivolapov, I. E. Kolesnikov, E. V. Grachova, S. P. Tunik, C. Bannwarth, S. Grimme, S. A. Katsyuba, A. A. Karasik, O. G. Sinyashin, *Dalton Trans.* **2016**, *45*, 2250.
[29] a) Y. Ma, C.-M. Che, H.-Y. Chao, X. Zhou, W.-H. Chan, J. Shen, *Adv. Mater.* **1999**, *11*, 852; b) C. Bizzarri, E. Spuling, D. M. Knoll, D. Volz, S. Bräse, *Coord. Chem. Rev.* **2018**, *373*, 49.
[30] a) H. D. Hardt, A. Pierre, *Z. Anorg. Allg. Chem.* **1973**, *402*, 107; b) H. D. Hardt, A. Pierre, *Inorganica Chim. Acta* **1977**, *25*, L59–L60.
[31] a) P. C. Ford, A. Vogler, *Acc. Chem. Res.* **1993**, *26*, 220; b) M. Vitale, W. E. Palke, P. C. Ford, *J. Phys. Chem.* **1992**, *96*, 8329; c) E. Lindsay, P. C. Ford, *Inorganica Chim. Acta* **1996**, *242*, 51.
[32] M. Zimmer, F. Rupp, P. Singer, F. Walz, F. Breher, W. Klopper, R. Diller, M. Gerhards, *Phys. Chem. Chem. Phys.* **2015**, *17*, 14138.
[33] S. Treiling, C. Wang, C. Förster, F. Reichenauer, J. Kalmbach, P. Boden, J. P. Harris, L. M. Carrella, E. Rentschler, U. Resch-Genger, C. Reber, M. Seitz, M. Gerhards, K. Heinze, *Angew. Chem. Int. Ed.* **2019**, *58*, 18075; *Angew. Chem.* **2019**, *131*, 18243.
[34] P. B. Becker, C. Förster, L. M. Carrella, P. Boden, D. Hunger, J. van Slageren, M. Gerhards, E. Rentschler, K. Heinze, *Chem. Eur. J.* **2020**, *26*, 7199.
[35] T. Yanai, D. P. Tew, N. C. Handy, *Chem. Phys. Lett.* **2004**, *393*, 51.
[36] X. Blase, C. Attaccalite, V. Olevano, *Phys. Rev. B* **2011**, *83*, 19158.
[37] K. Krause, W. Klopper, *J. Comput. Chem.* **2017**, *38*, 383.
[38] C. Holzer, W. Klopper, *J. Chem. Phys.* **2018**, *149*, 101101.
[39] A. J. Lees, *Comments Mod Chem. A Comments Inorg Chem.* **1995**, *17*, 319.
[40] a) R. P. Bell, *Proc. R. Soc. Lond. A* **1936**, *154*, 414; b) M. G. Evans, M. Polanyi, *Trans. Faraday Soc.* **1938**, *34*, 11; c) M. Nič, J. Jirát, B. Košata, A. Jenkins, A. McNaught (Eds.) *IUPAC Compendium of Chemical Terminology*, IUPAC, Research Triagle Park, NC, **2009**; d) *IUPAC Compendium of Chemical Terminology* (Eds.: M. Nič, J. Jirát, B. Košata, A. Jenkins, A. McNaught), IUPAC, Research Triagle Park, NC, **2009**.
[41] P. Müller, *Pure Appl. Chem.* **1994**, *66*, 1077.
[42] a) G. S. Hammond, *J. Am. Chem. Soc.* **1955**, *77*, 334; b) J. E. Leffler, *Science* **1953**, *117*, 340.
[43] R. Utrera-Melero, B. Huitorel, M. Cordier, J.-Y. Mevellec, F. Massuyeau, C. Latouche, C. Martineau-Corcos, S. Perruchas, *Inorg. Chem.* **2020**, *59*, 13607.
[44] G. D. Smith, M. S. Hutson, Y. Lu, M. T. Tierney, M. W. Grinstaff, R. A. Palmer, *Appl Spectrosc* **2001**, *55*, 637.
[45] O. V. Dolomanov, L. J. Bourhis, R. J. Gildea, J. A. K. Howard, H. Puschmann, *J. Appl. Crystallogr.* **2009**, *42*, 339.
[46] G. M. Sheldrick, *Acta Crystallogr. Sect. A* **2015**, *71*, 3.
[47] G. M. Sheldrick, *Acta Crystallogr. Sect. C* **2015**, *71*, 3.
[48] Gaussian 09, Revision D.01, M. J. Frisch, G. W. Trucks, H. B. Schlegel, G. E. Scuseria, M. A. Robb, J. R. Cheeseman, G. Scalmani, V. Barone, B. Mennucci, G. A. Petersson, H. Nakatsuji, M. Caricato, X. Li, H. P. Hratchian, A. F. Izmaylov, J. Bloino, G. Zheng, J. L. Sonnenberg, M. Hada, M. Ehara, K. Toyota, R. Fukuda, J. Hasegawa, M. Ishida, T. Nakajima, Y. Honda, O. Kitao, H. Nakai, T. Vreven, J. A. Montgomery, Jr., J. E. Peralta, F. Ogliaro, M. Bearpark, J. J. Heyd, E. Brothers, K. N. Kudin, V. N. Staroverov, T. Keith, R. Kobayashi, J. Normand, K. Raghavachari, A. Rendell, J. C. Burant, S. S. Iyengar, J. Tomasi, M. Cossi, N. Rega, J. M. Millam, M. Klene, J. E. Knox, J. B. Cross, V. Bakken, C. Adamo, J. Jaramillo, R. Gomperts, R. E. Stratmann, O. Yazyev, A. J. Austin, R. Cammi, C. Pomelli, J. W. Ochterski, R. L. Martin, K. Morokuma, V. G. Zakrzewski, G. A. Voth, P. Salvador, J. J. Dannenberg, S. Dapprich, A. D. Daniels, O. Farkas, J. B. Foresman, J. V. Ortiz, J. Cioslowski, D. J. Fox, Gaussian, Inc., Wallingfort, CT, **2013**.
[49] F. Furche, R. Ahlrichs, C. Hättig, W. Klopper, M. Sierka, F. Weigend, *WIREs Comput. Mol. Sci.* **2014**, *4*, 91.
[50] TURBOMOLE V7.4 2019, a development of University of Karlsruhe and Forschungszentrum Karlsruhe GmbH, 1989–2007, TURBOMOLE GmbH, since 2007; available from http://www.turbomole.com.
[51] a) S. Grimme, J. Antony, S. Ehrlich, H. Krieg, *J. Chem. Phys.* **2010**, *132*, 154104; b) S. Grimme, S. Ehrlich, L. Goerigk, *J. Comput. Chem.* **2011**, *32*, 1456.
[52] C. Holzer, W. Klopper, *J. Phys. Chem.* **2019**, *150*, 204116

[53] P. Plessow, *J. Chem. Theory Comput.* **2013**, *9*, 1305.
[54] a) D. Volz, T. Baumann, H. Flügge, M. Mydlak, T. Grab, M. Bächle, C. Barner-Kowollik, S. Bräse, *J. Mater. Chem.* **2012**, *22*, 20786; b) D. B. Grotjahn, D. A. Lev, *J. Am. Chem. Soc.* **2004**, *126*, 12232; c) Y. Li, S. Das, S. Zhou, K. Junge, M. Beller, *J. Am. Chem. Soc.* **2012**, *134*, 9727.

Manuscript received: October 11, 2020
Revised manuscript received: November 9, 2020
Accepted manuscript online: November 11, 2020
Version of record online: January 15, 2021

